Title

Structural signatures of the insulator-to-metal transition in $BaCo_{1-x}Ni_xS_2$

Journal

Physical Review Materials, 4(10)

ISSN

2475-9953

Authors

Schueller, Emily C
Miller, Kyle D
Zhang, William
et al.

Publication Date

2020-10-01

DOI

10.1103/PhysRevMaterials.4.104401

Peer reviewed

Structural signatures of the insulator-to-metal transition in $BaCo_{1-x}Ni_xS_2$

Emily C. Schueller,[1] Kyle D. Miller,[2] William Zhang,[1] Julia L. Zuo,[1]
James M. Rondinelli,[2] Stephen D. Wilson,[1] and Ram Seshadri[1,3]

[1]*Materials Department and Materials Research Laboratory, University of California, Santa Barbara, Santa Barbara, CA, 93106*
[2]*Department of Materials Science and Engineering, Northwestern University, Evanston, IL, 60208, USA*
[3]*Department of Chemistry and Biochemistry, University of California, Santa Barbara, Santa Barbara, CA, 93106*

(Dated: September 10, 2020)

The solid solution $BaCo_{1-x}Ni_xS_2$ exhibits an insulator-to-metal transition close to $x = 0.21$. Questions of whether this transition is coupled with structural changes remain open. Here we follow the structural evolution as a function of the Ni content x using synchrotron powder X-ray diffraction and pair distribution function analyses, to reveal significant basal sulfide anion displacements occurring preferentially along the CoS_5 pyramidal edges comprising the edge-connected bond network in $BaCo_{1-x}Ni_xS_2$. These displacements decrease in magnitude as x increases and are nearly quenched in $x = 1$ $BaNiS_2$. Density functional theory-based electronic structure calculations on $x = 0$ $BaCoS_2$ suggest that these displacements arise as a dynamic first-order Jahn-Teller effect owing to partial occupancy of nominally degenerate Co^{2+} d_{xz} and d_{yz} orbitals, leading to local structural symmetry breaking in the xy-plane of the Co-rich phases. The Jahn-Teller instability is associated with opening of a band gap that is further strengthened by electronic correlation. The Jahn-Teller effect is reduced upon increased electron filling as $x \to 1$, indicating local structure and band filling cooperatively result in the observed insulator-to-metal transition.

I. INTRODUCTION

The solid solution between $BaCoS_2$ and $BaNiS_2$ displays a compositionally driven insulator-to-metal transition when approximately 21% of the Co is replaced with Ni [1, 2]. The metallic end member, $BaNiS_2$, is a Pauli paramagnet with the tetragonal ($P4/nmm$) structure, exhibiting Ba layers alternating with layers of NiS_5 square pyramids [3]. $BaNiS_2$ has recently been reported to be a compensated semimetal with topological band crossings [4]. In the $P4/nmm$ space group, the NiS_5 square-pyramids are distorted such that the apical Ni–S bond lengths are slightly longer than the basal Ni-S lengths. The insulating end member $BaCoS_2$ displays antiferromagnetic order just above room temperature with a high spin Co^{2+} configuration [5]. $BaCoS_2$ has been reported to be a charge-transfer insulator with strong electron correlations [6, 7]. In $BaCoS_2$, there is a small monoclinic ($P2/c$) distortion to the compound in the plane of the layers, creating two unique bond lengths between the Co and the basal S [3]. However, unlike many known materials displaying insulator-to-metal transitions (for example, the dimerization of VO_2 [8–11]), the electronic transition in $BaCo_{1-x}Ni_xS_2$ has not been related to changes in the average or local structure. The monoclinic-to-tetragonal transition occurs for $0 \leq x \leq 0.1$, while the electronic transition does not occur until $x \approx 0.21$ [3, 12]. The insulator-to-metal transition is associated with the disappearance of magnetic order, although a small antiferromagnetic metal phase region has been reported [13]. This has led to speculation that the transition in $BaCo_{1-x}Ni_xS_2$ is purely electronic in origin [13, 14].

Here we study six compositions across the solid solution $BaCo_{1-x}Ni_xS_2$, corresponding to 3 insulating and 3 metallic phases, to understand the average and local structure evolution across the insulator-to-metal transition and the coupling with electronic and magnetic behavior. We employ high resolution synchrotron powder X-ray diffraction as well as X-ray pair distribution function data to probe both the average and local structure in each sample. Disordered local displacements from the average structure are observed, specifically on the basal S site, agreeing with previous reports of large atomic displacement parameters on that site in $BaCoS_2$ [3, 15]. Through reverse Monte Carlo (RMC) modeling of the average and local structure data, we find disordered basal S displacements along the edges of the square pyramids produce the best fit, and that the magnitude of the local displacements decreases significantly with Ni substitution.

An understanding of the origin of the local displacements on the basis of a first-order Jahn-Teller instability in $BaCoS_2$ (d^7) is obtained from density functional theory (DFT) calculations; the displacements appear to arise from an electronic degeneracy of the d_{xz} and d_{yz} orbitals that are fractionally occupied. These orbitals are fully occupied in $BaNiS_2$ (d^8), which explains the observed decrease in local distortions with increasing Ni. Although the average structure transition to $P2/c$ in $BaCoS_2$ slightly relieves the Jahn-Teller instability, calculations of the phonon dispersions indicate coherent soft mode instabilities in $BaCoS_2$ resulting in a $Pba2$ supercell with displacements of basal S atoms similar to those observed in the RMC modeling. These simulations suggest that the room temperature structure of $BaCoS_2$ and the other insulating members in the solid solution series with Ni may be a disordered version of this orthorhombic structure, analogous to the dynamically disordered Jahn-Teller distortions across the insulator-to-metal transition in Ca-doped $LaMnO_3$ [16].

II. METHODS

A. Computational Methods

First-principles spin-polarized density-functional theory (DFT) calculations on the $BaCoS_2$ end member were performed using the Vienna *Ab initio* Simulation Package (VASP) [17] with projector-augmented-wave pseudopotentials [18, 19] within the Perdew–Burke–Ernzerhof generalized gradient approximation (PBE) [20] for band structure calculations and the version revised for solids (PBESol) [21] for phonon calculations). For all calculations, we use a 600 eV plane wave cutoff and treat the core and valence electrons with the following electronic configurations: $5s^2 5p^6 6s^2$ (Ba), $3d^8 4s^1$ (Co), and $3s^2 3p^4$ (S). We sample the Brillouin zone with a Γ-centered k-point mesh with a density of 864 k-points per reciprocal atom.

Our structures are obtained by full ionic relaxation within three model space groups, the idealized $P4/nmm$ which we use as a reference structure for analysis of the lattice dynamics and orbital filling, and two symmetries derived as small distortions to the ideal structure. The two distorted space groups are $P2/c$ and $Pba2$, the former best describing the average structure and the latter best describing the anomalous sulfide displacements. All relevant structure files are provided in the the Supplemental Material (SM) [22].

All calculations were initialized with a collinear antiferromagnetic spin order, consistent with the experimental ground state [5] using 3 μ_B on each Co site. We also use a Hubbard U correction following the Dudarev *et al.* approach [23] with $U_{\text{eff}} = 2$ eV on the correlated Co $3d$ manifold, notably smaller than in previous studies [24]. We chose this strength of static Coulomb interaction because it provides the best band gap agreement to that estimated from room temperature transport measurements in Mandrus *et al.* [5] when using the average experimental $P2/c$ structure (see SM Figure S3 [22]). In addition to matching the $x = 0$ end member, we also found that for all values of $U_{\text{eff}} \in [0, 4]$ eV, our DFT-PBE+U_{eff} approach correctly predicts a metallic state for the nonmagnetic $x = 1$ end member $BaNiS_2$ (see SM Figure S4 [22]).

We used the Phonopy package with a $2 \times 2 \times 1$ supercell for pre- and post-processing of the dynamical matrix [25]. We parsed and visualized our computational results with the Python package pymatgen [26].

B. Experimental Methods

$BaCo_{1-x}Ni_xS_2$ powder was obtained by solid state reaction of BaS (Sigma Aldrich, 99.9%), Co, Ni, and S powders. The Co powder was reduced under flowing 5% H_2 in Ar at 800 °C for 12 hours to remove surface oxides. Stoichiometric amounts totaling around 500 mg of the starting materials were ground with an agate mortar and pestle and pressed into a 6 mm pellet under 950 MPa of pressure. For Co-containing members, the pellets were placed in Al_2O_3 crucibles to prevent reaction with the fused silica tubes. The samples were sealed in fused silica tubes under vacuum with 0.25 atm partial pressure of Ar to suppress S volatilization. $BaNiS_2$ was heated at 820°C and $BaCoS_2$ was heated at 970°C, and the intermediate compositions were reacted at temperatures linearly interpolated between the end members. All compounds were reacted for 1.5 days and then quenched in water. For the Co-containing compounds, the silica tube and alumina crucible had to be quenched separately in a 2-step process to achieve a fast enough quench to avoid decomposition. All compounds were screened by laboratory Cu-Kα X-ray diffraction (XRD) to check for impurities. Only minor $BaSO_4$ or BaS impurities of less than 5%, confirmed by synchrotron diffraction, could be identified in each compound.

High resolution synchrotron powder X-ray diffraction was performed at the Advanced Photon Source at Argonne National Laboratory at the 11-BM beamline. Approximately 30 mg of powder was loaded into a kapton capillary and measured for 1 hour at room temperature. Rietveld refinements were performed using the TOPAS analysis package [27]. Crystal structures were visualized using the VESTA software suite [28].

Pair distribution function measurements were performed at the Advanced Photon Source at Argonne National Laboratory at the 11-ID-B beamline. Approximately 30 mg of powder was loaded into a kapton capillary and measured for 1 hour at room temperature. The data were integrated using calibration with a CeO_2 standard via Fit2D [29] and Fourier transformations into real space were performed using PDFgetX3 [30]. Small box modeling at various r-ranges was performed using PDFgui [31] and large box modeling of both the diffraction and pair distribution function data was performed with RMCprofile [32]. RMCprofile results were analyzed with the python package pymatgen [26]. The order parameter of the square pyramidal coordination environments within the supercell were calculated using the pymatgen local environment package with the local structure order parameter function [26].

Bulk magnetic measurements were performed on a Quantum Design MPMS 3 SQUID Vibrating Sample Magnetometer, with approximately 30 mg of powder loaded into a plastic container and mounted in a brass holder. Temperature-dependent magnetization measurements from $T = 2$ K to $T = 350$ K were performed upon warming under zero-field-cooled and field-cooled conditions with an applied field of $H = 200$ Oe. Resistivity measurements were performed on bar pellets which were sintered using the aforementioned reaction conditions. The measurements were performed in a Quantum Design PPMS using a press–contact setup for a 4-point measurement with standardized contact spacing. Measurements were taken on warming from $T = 2$ K to $T = 300$ K at a 0.5 K/min sweep rate to avoid temperature hysteresis.

X-ray fluorescence measurements were performed on a

Rigaku ZSX Primus IV spectrometer on pressed pellets of the powder material to confirm Co/Ni ratios in samples across the solid solution.

III. RESULTS AND DISCUSSION

We prepared 6 polycrystalline samples across the series $BaCo_{1-x}Ni_xS_2$ (x = 0, 0.1, 0.15, 0.25, 0.5, 1), 3 insulators (x <0.21) and 3 metals. Temperature–dependent resistivity on sintered pellets, shown in Figure 1(a), confirms the presence of an insulator-to-metal transition between x=0.15 and x=0.25. Temperature–dependent magnetization with an applied field of H = 200 Oe, shown in Figure 1(b) demonstrates suppression of the Néel temperature with increasing Ni in the insulating members and Pauli paramagnetic behavior in the metallic members, consistent with previous reports [1]. Muon spin resonance studies have suggested the transition proceeds through an intermediate antiferromagnetic metal phase [13], but we did not explore compositions in this region. The slight inconsistencies in magnetic susceptibility are likely due to trace cobalt oxide impurities. While the properties data indicates that the sample compositions are close to the nominal compositions, we also checked the ratio of Co:Ni in the intermediate members with X-ray fluorescence (XRF) measurements, shown in the SM Table S1 [22]. Our XRF results confirm the ratio of metals in the products are very similar to the nominal compositions, so we use the nominal compositions throughout.

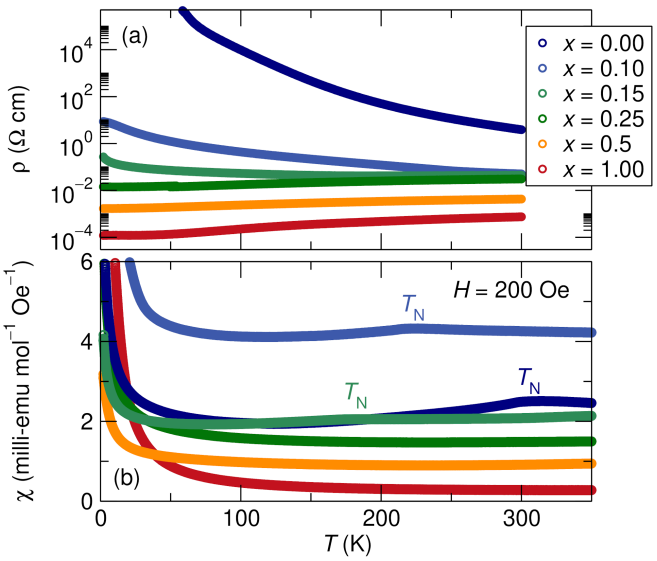

FIG. 1. (a) Temperature–dependent resistivity measurements on $BaCo_{1-x}Ni_xS_2$ [values of x indicated in panel (a)] point to an insulator-to-metal transition between x = 0.15 and x = 0.25, indicated by a change of slope in the resistivity with temperature, consistent with a reported critical Ni fraction of x = 0.21. (b) Temperature–dependent magnetization measurements on $BaCo_{1-x}Ni_xS_2$ reveal a suppression of the Néel temperature (T_N) with increasing x until the insulator-to-metal transition, beyond which no magnetic ordering is seen. A magnified trace of the susceptibility for x = 0.15 is shown in SM Figure S1 [22] for a clearer view of the magnetic transition.

The $BaCo_{1-x}Ni_xS_2$ crystal structure is characterized by layers of Ba atoms alternating with layers of M–S (M = Co,Ni) square pyramids. In all Ni-containing members of the series, the average structure is tetragonal ($P4/nmm$), with the apical M–S bond length distinct from the 4 basal M–S bonds. In the $BaCoS_2$ end member, the tetragonal structure undergoes a small distortion into a monoclinic ($P2/c$) space group, splitting the 4 basal M–S bond lengths into 2 sets of 2 equivalent bonds lengths. As shown in Figure 2, the basal S atomic displacement parameters (ADPs) are elevated across the solid solution, especially in the low-x members, indicating large site disorder.

The difficulty in achieving high quality fits to the diffraction data with the $P2/c$ structural model in addition to the large and highly anisotropic sulfide ADPs suggests large local distortions are occurring which are disordered at room temperature. Figure 3 shows changes in the average structure across the solid solution. As the amount of Ni increases, both the unit cell and the M–S square pyramids become less distorted, approaching a pseudo-cubic structure near x = 0.5. The ADPs, shown in Figure 3(d), are larger for the basal S and Co on the Co-rich side compared to the apical S and they decrease upon increasing Ni concentration, suggesting local distortions decrease across the solid solution. The apical S ADPs are relatively constant across the solid solution, suggesting that site is relatively unperturbed by the differences in electronic structure between Co^{2+} and Ni^{2+}. Anomalously large ADPs on the basal S site have been noted in the literature [15], but an explanation has not yet been proposed.

In order to look for local disorder across the series, which may explain the composition-dependent ADPs, we next perform room temperature powder X-ray pair distribution function (PDF) analyses. PDF data is obtained *via* a Fourier transform of total scattering data which provides a histogram of atom-atom distances in a material, making it useful to uncover local spatial or dynamic distortions. From an examination of the PDF data in the Co-rich members (Figure 4), we find an asymmetry of the lowest-r peak around r=2.4 Å, which corresponds to M–S bonds within a square pyramid. The asymmetry becomes less prominent with increasing Ni content. The high-r tail of this peak corresponds with longer bond lengths than were found in the average structure, suggesting that locally the square pyramids are distorting but not in an ordered fashion. This significant asymmetry is poorly fit even with monoclinic $P2/c$ symmetry (the average structure of $BaCoS_2$), indicating that the local S displacements in the M–S square pyramids are incompatible with $P2/c$ symmetry.

For the mid-r ranges from about r = 5 Å to r = 10 Å, we find that the monoclinic structure gives a better fit than the tetragonal structure, as determined by examination of the difference curve. This improvement is stronger in

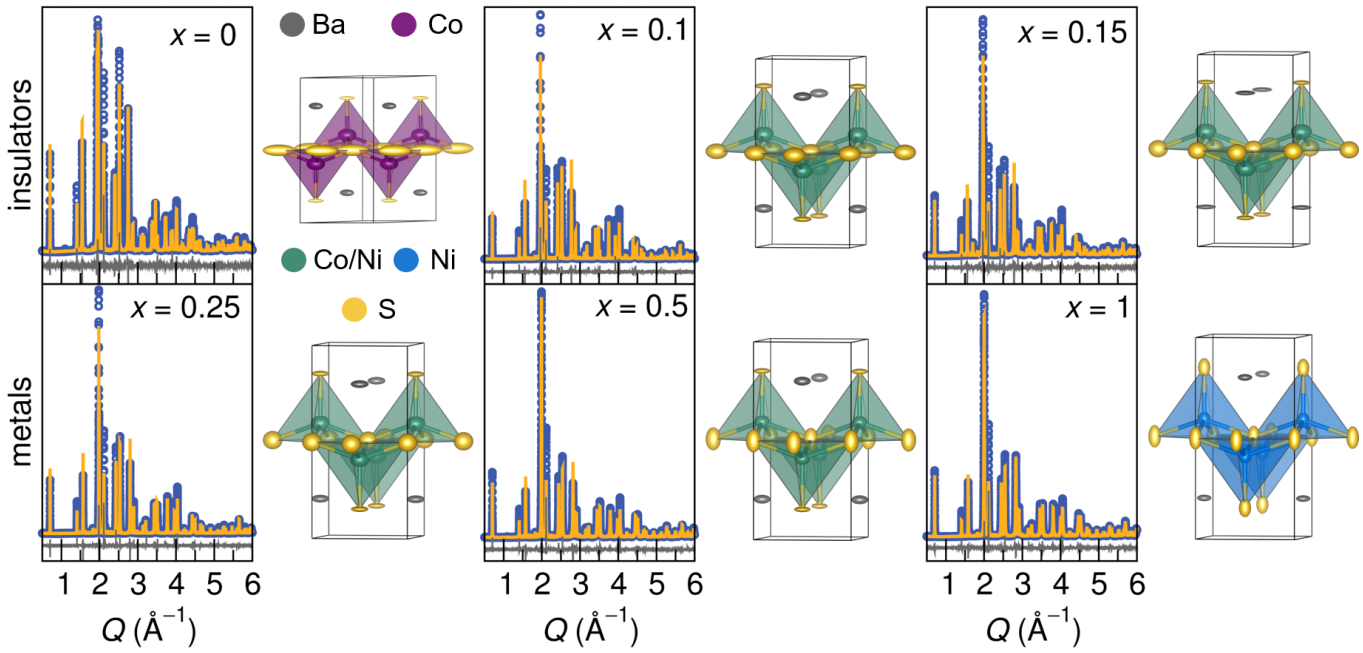

FIG. 2. Synchrotron diffraction fits and their associated crystal structures across the solid solution from $BaCoS_2$ to $BaNiS_2$ show large basal S atomic displacement parameters (ADPs), indicating a high level of disorder on that site. Additionally, slight peak height discrepancies in the fits indicate our average structure $P2/c$ model cannot fully capture the complexities of the crystal structure. The ADPs are shown as 99% probability ellipsoids. Crystallographic tables can be found in SM Table S2. [22].

samples with higher Co-content, even in samples where the average structure is tetragonal. In order to better understand these trends, we performed additional fits up to $r = 30$ Å with both space groups. We attempted to capture the unit-cell level square pyramidal distortions by limiting the fit range to $r = 5$ Å, but there were too many parameters in the monoclinic structure to obtain a statistically significant fit without highly correlated variables. Furthermore, the lowest-r distortions (<5 Å) did not appear to be compatible with $P2/c$ symmetry and gave unphysical basal S ADPs.

By comparing parameters from fits to the tetragonal and monoclinic space groups as well as comparing fits across length scales, we propose a model for the local structure as well as the short-range order length scale in $BaCo_{1-x}Ni_xS_2$. In Figure 5, we find that regardless of the space group or fit range, we recover qualitatively similar average structure trends across the solid solution, showing a reduction in distortion with increasing x. Interestingly, low-x samples are more sensitive to the space group and fit-range used than high-x samples. This indicates that for Ni-rich samples, the local structure is relatively consistent across multiple length scales and is consistent with the average structure. For the Co-rich samples, bond lengths and distortion levels within a square pyramid, shown in Figure 5(a) and (b), are strongly dependent on the structural model and length-scale of fitting, indicating local square pyramidal distortions at various length scales.

One of the largest changes across the solid solution is the ADP for the basal S. From the fit of the average structure from the diffraction data, the magnitude of the basal S ADP decreases as x increases. In the PDF data, from Figure 5(c) we find not only this trend, but additionally that the basal S ADP is larger at lower r-ranges as well as when we allow the symmetry to reduce to monoclinic. This further suggests that the local distortions in $BaCo_{1-x}Ni_xS_2$ are dominated by displacements of the basal S from its crystallographic site.

Finally, the weighted R-parameter, a metric for the goodness-of-fit shown in Figure 5(d), indicates that the monoclinic structure always fits the PDF data better than the tetragonal structure, which is unsurprising considering the monoclinic structure has more parameters. However, the monoclinic structure improves the fit more substantially on the Co-rich side. Additionally, the effect is stronger in the 10 Å fits than the 30 Å fits, corroborating the observation that the distortions are local and correlations weaken with increasing r. Together, the diffraction and PDF data hint at significant local displacements in the low-x region of the solid solution, with the basal S likely to be the source of these displacements.

We next perform large-box reverse Monte Carlo (RMC) modeling implemented in RMCprofile, which simultaneously fits the average and the local structure data to examine the local displacements without symmetry constraints imposed by a particular structural model. RMCprofile is initialized with a supercell generated from the average structure which is evolved *via* random displacements towards an improvement of the fit of both

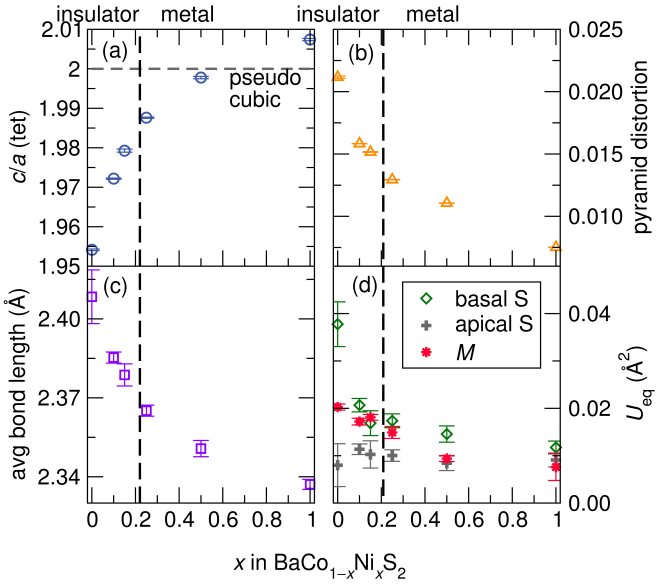

FIG. 3. (a) The c/a ratio approaches the pseudo-cubic value of 2 as $x \to 1$ in $BaCo_{1-x}Ni_xS_2$. (b) The distortion of the square pyramid, related to the difference between the apical and the basal M–S bond length, decreases with increasing Ni content. (c) The average M–S bond length decreases with increasing x. (d) Basal S and Co ADPs decrease across the solid solution, indicating less distortions on those sites with increasing Ni. The apical S ADPs are relatively composition independent.

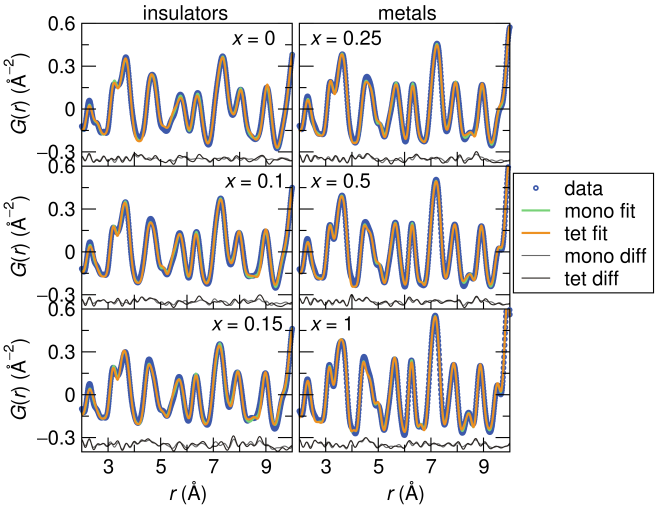

FIG. 4. PDF data fit to $r = 10$ Å with a monoclinic and tetragonal space group. In the Co-rich phases, there is a distinct asymmetry on the first peak (corresponding to M–S bonds within the square pyramid) that is difficult to fit even with the monoclinic space group, suggesting distortions of the square pyramids not compatible with $P2/c$ symmetry. At mid-r ranges, the monoclinic fit outperforms the tetragonal fit, especially in the Co-rich phases, indicating solid-solution compositions exhibiting an average tetragonal symmetry also have local distortions.

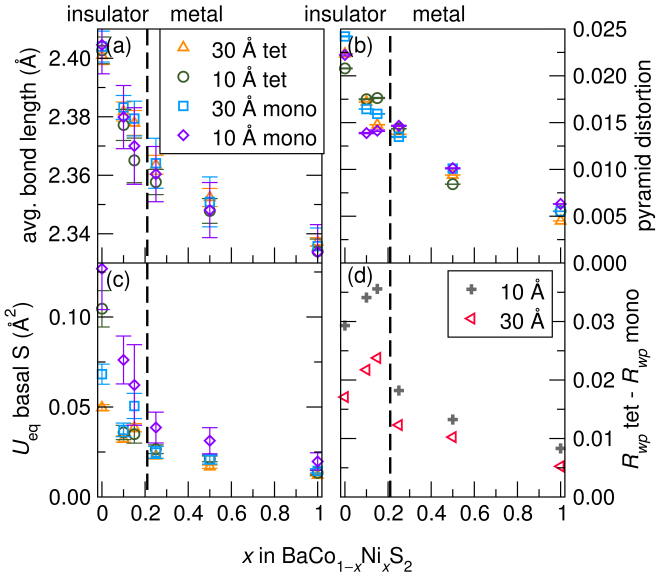

FIG. 5. (a) Average bond length and (b) square pyramidal distortion across the $BaCo_{1-x}Ni_xS_2$ solid solution show a strong dependence on fit range and space group model for low-x compounds, but converge as x increases, indicating less local distortion in the Ni-rich samples. (c) Basal S ADPs diverge at low-x even when fitting with a monoclinic structure, indicating the basal S atoms are locally displacing from their ideal crystallographic sites. (d) The difference in the weighted-R parameter between the tetragonal and monoclinic structure shows the lower symmetry structure is required to accurately describe the local structure of the insulating samples. Additionally, the distortions are more prominent in the low-r fits, indicating the short-range order begins to disappear by 30 Å.

the PDF and the diffraction data. By performing multiple repetitions of these calculations, we generate a set of displacements which reproducibly fit both the diffraction and PDF data. By initializing the calculation with a $10 \times 10 \times 10$ (8,000 atom) supercell and repeating the simulation 3 times with different arrangements of the Co and Ni atoms each time in the intermediate phases, we can capture the local structure evolution with Ni content.

Figure 6(a) shows a typical fit to the diffraction and PDF data for $x = 0$. The supercell reproduces the significant distortions in the local coordination environment of the M site (the shoulder in the first M–S peak) while also fitting the higher-r local structure and the diffraction data. The supercells collapsed back into their average structure unit cells are shown in Figure 6(b), providing a visualization of the difference between the average and local structure across the series. Consistent with ADP data from small box modeling, the most striking displacements occur on the basal S sites. The displacements occur within the plane of the square pyramid, with a preference for displacements along the edges of the square pyramids. These displacements break symmetry in the plane of the square pyramids and allow for the formation of longer M–S bond lengths, as seen in the low-r PDF data. Additionally, because the displacements lack long-range order,

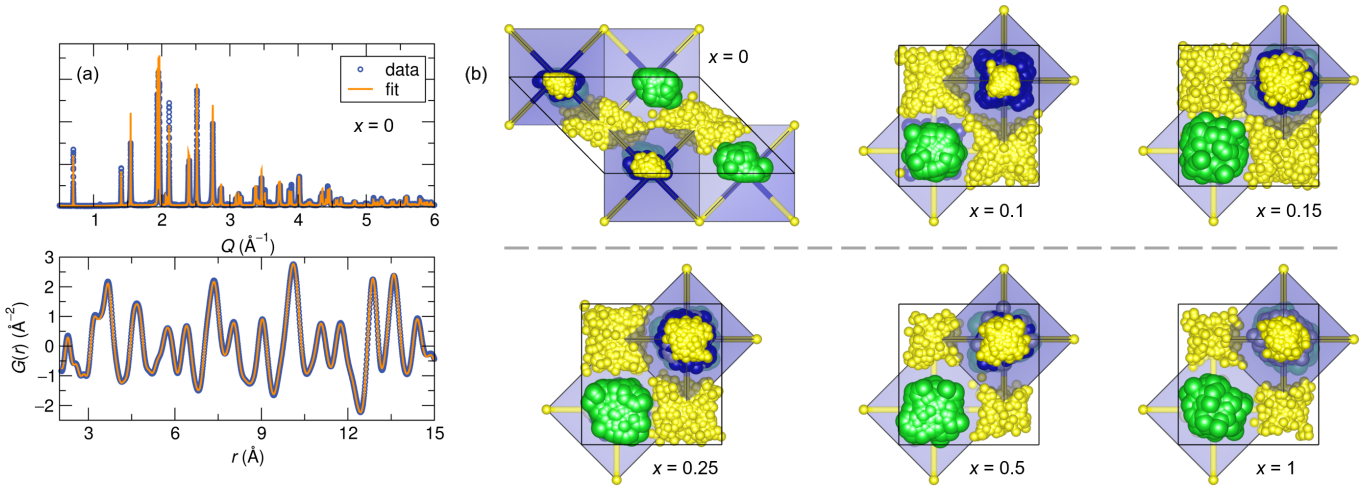

FIG. 6. (a) Reverse Monte Carlo modeling is able to generate a structure that fits the diffraction and PDF data simultaneously, including the significant low-r distortions in the x=0 PDF data. (b) Collapsing the Monte Carlo supercells into the average structure unit cell shows the tendency of basal S atoms to locally displace along the edges of the square pyramids. This displacement allows for symmetry breaking in the plane of the square pyramid which is evident in the PDF data, and is more pronounced in the insulating compounds. The disordered nature of the displacements spatially averages over several unit cells, creating the higher symmetry diffraction patterns.

the average structure appears to be of higher symmetry, as seen in the diffraction data.

Analysis of the square pyramidal coordination environment for each supercell provides insight into how the symmetry of the M-site changes across the series. The square pyramidal distortion from RMC modeling, shown in Figure 7(a), decreases with increasing Ni, consistent with trends from Rietveld refinements and small box PDF modeling. The error bars indicate the standard deviation in distortion for the 6,000 coordination polyhedra across the supercells at each composition. The large magnitude of the error bars indicates that there is a wide variance in polyhedral distortion across the supercell. While some Co or Ni are located in relatively high symmetry coordination environments, others are located in extremely distorted sites. The X-ray scattering factors from Co and Ni are too similar to distinguish Ni–S and Co–S polyhedra, but additional studies could probe whether the Ni–S pyramids tend to be less distorted than the Co–S pyramids in the intermediate members. To compare the RMC results with Rietveld and small-box modeling, the maximum and minimum bond length in the square pyramid are plotted in Figure 7(b) with error bars for the RMC showing the standard deviation across the supercell, similar to Figure 7(a). Although the maximum and minimum bond lengths converge towards an ideal square pyramid as x increases in all 3 techniques, the RMC modeling stabilizes more significant distortions by allowing disorder and reducing the symmetry to $P1$.

In both the tetragonal and monoclinic structures, the Wyckoff site of the basal S anions lacks in-plane degrees of freedom, such that the local structure displacements observed from our reverse Monte Carlo simulations are incompatible with the space group of the average structure. Such symmetry-breaking in $BaCoS_2$ may originate from any combination of (i) orbital, (ii) defect-derived, or (iii) magnetic driving forces. First, we examine an electronic instability as the origin for the aforementioned displacements. Owing to the $S = 3/2$ Co^{2+} configuration, three electrons occupy two degenerate d_{xz} and d_{yz} orbitals [33], which leads to a first-order Jahn-Teller (FOJT) instability of the CoS_5 polyhedron that may be removed by symmetry breaking in the xy-plane (Figure 8). The edge-connectivity in the (001) plane restricts sulfide displacements directed along the Co–S bond; they cannot coherently occur without changing the bond network.

When modeling structural phase transitions driven by phonon instabilities [34–36], soft phonons or those with imaginary frequencies are useful for finding displacive transitions. Phonon modes with $\nu^2 < 0$ computed for a structure indicate that the phase is dynamically unstable; it will spontaneously distort into a lower symmetry structure. Such instabilities also appear in the potential energy surface as regions of negative curvature when expanded with respect to these soft modes because $d^2E/dr^2 < 0 \propto \nu^2$.

We ascertain the energy stabilizing displacements that both alleviate the first-order Jahn-Teller instability and are compatible with the square pyramidal connectivity by performing first-principles phonon calculations on the ideal tetragonal structure with $P4/nmm$ symmetry (Figure 9(a)). Although we find experimentally a monoclinic $P2/c$ symmetry with an interaxial angle $\gamma \neq 90°$, arising from a small shearing of the basal plane of the square pyramids, we remove this feature to isolate the degeneracy-lifting effect of the basal S displacements. We find a pair of degenerate modes with $\nu_{1,2} = 3.1i$ THz at the M-point ($k = (\frac{1}{2}, \frac{1}{2}, 0)$, Figure 9(a)). Each individ-

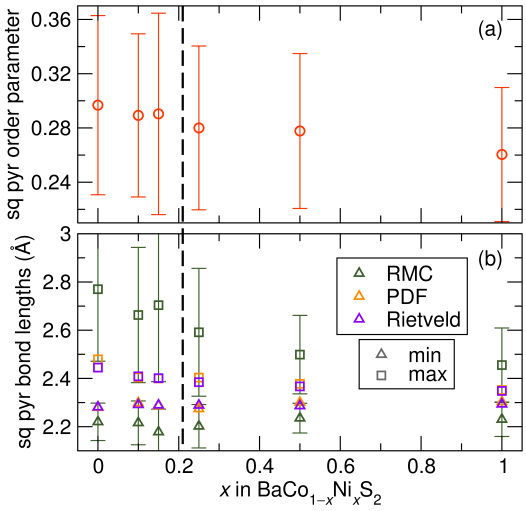

FIG. 7. (a) The reverse Monte Carlo (RMC) fits show the square pyramidal distortion decreases as x increases, similar to the results of Rietveld refinement and small box modeling. The error bars for the RMC results represent the standard deviation of the pyramidal distortion across the supercell, indicating a large variance in the square pyramid distortions consistent with disorder on the basal S site. (b) Comparison of square pyramidal bond lengths in the Rietveld refinement, small box PDF, and RMC modeling. Although the trends are similar across all three techniques – a convergence of bond lengths towards an ideal square pyramid – the removal of symmetry constraints with RMC allows for a larger amount of distortion as well as variance in distortion. Error bars on Rietveld and small box PDF refinements are shown in earlier figures and omitted here for clarity.

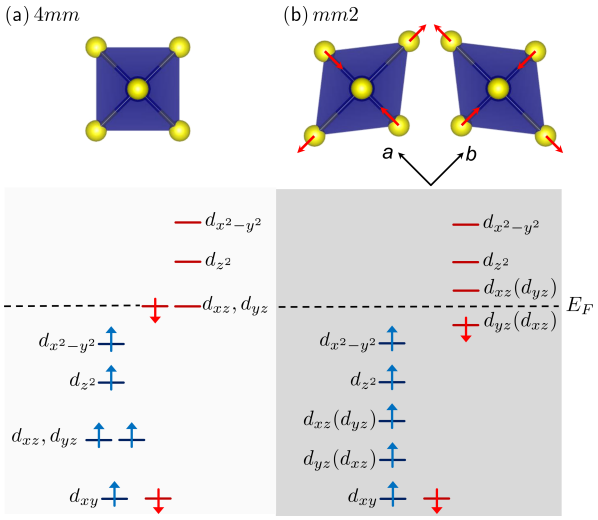

FIG. 8. The first-order Jahn-Teller instability arising from (a) the degeneracy of the d_{xz} and d_{yz} spin down orbitals within the CoS_5 square pyramids can be relieved by (b) removal of the fourfold symmetry of the ideal polyhedron.

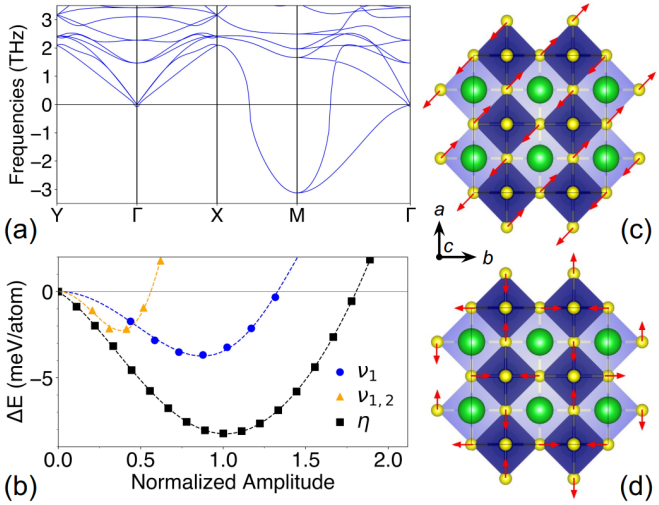

FIG. 9. (a) The phonon dispersions in the $k_z = 0$ plane of the $P4/nmm$ $BaCoS_2$ structure reveal imaginary (negative) modes at the M point. (b) Energy calculations for structures as a function of the normalized distortion-mode amplitudes (see text), for ν_1, $\nu_{1,2}$, and η, where $\eta = 0$ and $\eta = 1$ correspond to the relaxed $P4/nmm$ and $Pba2$ structures, respectively. Illustration of the basal sulfide displacements in the a-b plane corresponding to (c) the unstable phonon $\nu_1 = 3.1i$ THz and (d) the combination of the two degenerate modes $\nu_{1,2}$. Note that ν_2 is equivalent to ν_1 rotated by 90°.

ual mode comprises displacements of basal sulfide anions along the pyramidal edges, shown in Figure 9(c), whereas their combination leads to basal S displacements along the Co-S bonds (Figure 9(d)). All displacement patterns transform as the two-dimensional irreducible representation M_4, cause a $P4/nmm \rightarrow Pba2$ symmetry reduction, and lift the d_{xz} and d_{yz} orbital degeneracy. Although the $\nu_{1,2}$ distortion pattern is more typical of the FOJT in layered structures, Figure 9(b) shows that the sulfide displacements along the pyramidal edges (ν_1) are more energetically favorable than those along the Co–S bonds ($\nu_{1,2}$). This dependence is likely due to the reduced elastic energy cost of displacing the basal S diagonally to rather than along the Co–S bonds.

Next, we relaxed $BaCoS_2$ initialized in this $Pba2$ symmetry and find that it is derived from the tetragonal structure according to the distortion-mode $\eta = 0.98\xi(\nu_1) + 0.13\xi(\nu_2) + 0.15\xi(\Gamma_1^+)$. The dominance of the $\xi(\nu_1)$ coefficient indicates that the displacements ξ comprising η are almost entirely derived from the ν_1 mode with only minor contributions from ν_2 and the fully symmetric mode. The relaxed $Pba2$ structure exhibits basal S displacements along the pyramidal edges, in agreement with the experimentally observed local distortions, and is 8 meV/atom lower in energy than the the $P4/nmm$ structure, shown in Figure 9(b).

The effect of these energy lowering basal S displacements on the electronic structure is presented in Figure 10. The metallic antiferromagnetic $P4/nmm$ phase transforms into a semiconducting $Pba2$ phase owing to

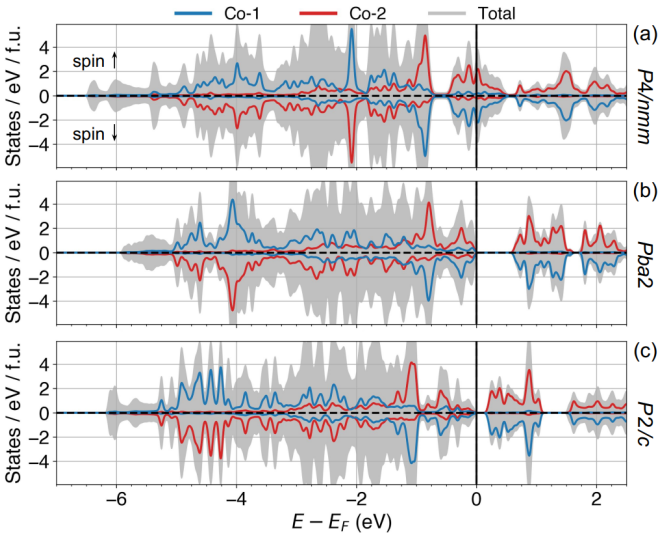

FIG. 10. Projected DOS for the (a) $P4/nmm$, (b) $Pba2$, and (c) $P2/c$ structures. For (a) and (c), the minority-spin d_{xz} and d_{yz} states span [-2.5, 1] eV whereas in the minority-spin channel for (b), the d_{xz} state spans [-3.0 eV,VBM] and the d_{yz} state spans [CBM, 1.5 eV]. CBM refers to the conduction band minimum and VBM refers to the valence band maximum. Although $P2/c$ and $Pba2$ both remove the degeneracy of d_{xz} and d_{yz}, lowering the density of states at the Fermi level, the $Pba2$ symmetry breaking is more significant and opens a gap with $U_{\text{eff}} = 2$ eV. Total (gray) and projections onto majority spin-up (blue) and majority spin-down (red) cobalt species are shown. Electronic band structures near the Fermi level are shown in SM Figure S2 [22].

the removal of the orbital degeneracy. Figure 10(a) shows d_{xz} and d_{yz} states crossing the Fermi level in the $P4/nmm$ structure whereas $Pba2$ features d_{xz} preferentially and fully occupied over the d_{yz} orbital (Figure 10(b)). Although the $P2/c$ monoclinic distortion similarly lifts the d_{xz} and d_{yz} orbital degeneracy with $U_{\text{eff}} = 2$ eV (Figure 10(c)), the symmetry breaking only opens a small 0.15 eV gap compared to the much larger 0.68 eV gap in the $Pba2$ structure exhibiting basal sulfide displacements. Furthermore, our electron doping simulations show that the band gap persists at much higher doping levels for the $Pba2$ structure than for the $P2/c$ structure (see SM Figure S5). This behavior indicates that although electron filling is essential to driving the IMT, changes in atomic structure determine the critical Ni concentration. Our identified interdependence of the band gap on the basal S displacements suggests that the FOJT instability helps drive the insulator-to-metal transition in the $BaCo_{1-x}Ni_xS_2$ system. Upon electron doping with Ni in the solid solutions, the additional electron will occupy the d_{xz} and d_{yz} orbitals completely, removing the instability. Indeed for $x = 1$ $BaNiS_2$, the atomic displacement parameters converge to reasonable values on all sites in the Rietveld refinement and PDF small box modeling, and both the tetragonal structure and monoclinic structure fit the PDF data equally well. From our RMC modeling on the $BaNiS_2$ end member, we find a convergence of bond lengths within the NiS_5 polyhedra to similar values, indicating less distortion, and in the collapsed supercell, we find smaller displacements from the ideal crystallographic sites.

Alternative symmetry-breaking of the average structure that may produce anomalous ADPs could be due to sulfur vacancies, which have been found in $BaCoS_2$[3]. Sulfur vacancies of sufficient concentrations, however, would also trigger a temperature dependent insulator-to-metal transition in $BaCo_{0.9}Ni_{0.1}S_{2-y}$ for $0.05 \leq y \leq 0.20$ [37], which we do not observe in our data, ruling out the possibility of sulfur vacancies as the origin of the anomalous ADPs.

Another scenario could involve magnetism. In the monoclinic structure ($P2/c$), the AFM ordering produces the magnetic space group P_a2/c, no. 13.70, which lowers the basal S site symmetry from $2f$ $(\frac{1}{2}, y, \frac{1}{4})$ to $8g$ (x, y, z), allowing in-plane displacements. However, since the local distortions persist in the paramagnetic phases of $BaCo_{1-x}Ni_xS_2$, the magnetic ordering cannot be the primary driving force for local M_4 displacements; the additional degrees of freedom from the antiferromagnetic order likely play an auxiliary role in generating the displacements.

IV. CONCLUSION

In the insulating members of the $BaCo_{1-x}Ni_xS_2$ solid solution, disorder on the basal S site leads to local symmetry breaking in the plane of the square pyramid. In the square pyramidal configuration, the high-spin Co^{2+} ion has doubly degenerate d_{xz} and d_{yz} orbitals which are partially filled by 3 electrons, leading to a Jahn-Teller instability. In the $BaCoS_2$ end member, the Jahn-Teller degeneracy appears to be relieved by two separate structural mechanisms – an average structure distortion to the monoclinic $P2/c$ and a local structure distortion of basal S atoms along the edges of the square pyramids. Because only the local structure distortions are observed at room temperature in the paramagnetic insulating compounds, it is possible that the formation of the $P2/c$ structure in $BaCoS_2$ is related to the antiferromagnetic order. Rietveld refinement, PDF small box modeling, and RMC modeling show that the local S displacements decrease as x increases, consistent with the additional electron in Ni filling the d_{xz} and d_{yz} orbitals completely and removing the instability.

While the average structure of $P2/c$ slightly breaks the in-plane symmetry in $BaCoS_2$, we find that the basal S displacements along the pyramidal edges (as in a $Pba2$ structure) further lift this symmetry, widening the band gap between the Jahn-Teller active d_{xz} and d_{yz} states. We hypothesize that at room temperature, $BaCoS_2$ prefers a dynamically disordered version of the $Pba2$ or similar structure due to the small energy differences (<10 meV/atom) separating the M_4-symmetry adapted S displacements, the $P2/c$ structure, and the $P4/nmm$ structure. From

a combination of DFT-based modeling and average and local structure analysis, we find that local Jahn-Teller distortions associated with certain band fillings, in the presence of static electron correlation, drive the insulator-to-metal transition in the $BaCo_{1-x}Ni_xS_2$ system. This work strengthens the emerging understanding that following structural changes in great detail is essential for determining the physical underpinnings of insulator-to-metal transitions.

ACKNOWLEDGMENTS

This research was supported by the National Science Foundation under DMREF Awards DMR-1729489 and DMR-1729303. Use of the Shared Experimental Facilities of the Materials Research Science and Engineering Center (MRSEC) at UC Santa Barbara (DMR 1720256) is gratefully acknowledged. The UC Santa Barbara MRSEC is a member of the NSF-supported Materials Research Facilities Network (www.mrfn.org). We also acknowledge support from the Center for Scientific Computing from the CNSI, MRL: an NSF MRSEC (DMR-1720256) and NSF CNS-1725797, as well as the National Energy Research Scientific Computing Center, a DOE Office of Science User Facility supported by DOE DE-AC02-05CH11231. This research was also supported in part through the computational resources and staff contributions provided for the Quest high performance computing facility at Northwestern University which is jointly supported by the Office of the Provost, the Office for Research, and Northwestern University Information Technology. Use of the Advanced Photon Source at Argonne National Laboratory was supported by the U. S. Department of Energy, Office of Science, Office of Basic Energy Sciences, under Contract No. DE-AC02-06CH11357.

[1] J. Takeda, Y. Kobayashi, K. Kodama, H. Harashina, and M. Sato, Transport, Magnetic and Thermal Properties of $BaCo_{1-x}Ni_xS_2$, J. Phys. Soc. Jpn. **64**, 2550 (1995).

[2] M. Sato, H. Sasaki, H. Harashina, Y. Yasui, J. Takeda, K. Kodama, S. Shamoto, K. Kakurai, and M. Nishi, Metal–Insulator Transition of $BaCo_{1-x}Ni_xS_2$ Induced by Pressure and Carrier Number Control, Rev. High Pressure Sci. Technol. **7**, 447 (1998).

[3] L. S. Martinson, J. W. Schweitzer, and N. C. Baenziger, Properties of the Layered $BaCo_{1-x}Ni_xS_2$ Alloy System, Phys. Rev. B **54**, 11265 (1996).

[4] Y. Klein, M. Casula, D. Santos-Cottin, A. Audouard, D. Vignolles, G. Fève, V. Freulon, B. Plaçais, M. Verseils, H. Yang, L. Paulatto, and A. Gauzzi, Importance of Nonlocal Electron Correlation in the $BaNiS_2$ Semimetal from Quantum Oscillations Studies, Phys. Rev. B **97**, 075140 (2018).

[5] D. Mandrus, J. L. Sarrao, B. C. Chakoumakos, J. A. Fernandez-Baca, S. E. Nagler, and B. C. Sales, Magnetism in $BaCoS_2$, J. Appl. Phys. **81**, 4620 (1997).

[6] K. Takenaka, S. Kashima, A. Osuka, S. Sugai, Y. Yasui, S. Shamoto, and M. Sato, Anisotropic Optical Spectra of $BaCo_{1-x}Ni_xS_2$: Effect of Ni Substitution on the Electronic Structure of the $Co_{1-x}Ni_xS$ Plane, Phys. Rev. B **63**, 115113 (2001).

[7] D. Santos-Cottin, Y. Klein, P. Werner, T. Miyake, L. de'Medici, A. Gauzzi, R. P. S. M. Lobo, and M. Casula, Linear Behavior of the Optical Conductivity and Incoherent Charge Transport in $BaCoS_2$, Phys. Rev. Materials **2**, 105001 (2018).

[8] J. B. Goodenough, Direct Cation–Cation Interactions in Several Oxides, Phys. Rev. **117**, 1442 (1960).

[9] J. P. Pouget, H. Launois, J. P. D'Haenens, P. Merenda, and T. M. Rice, Electron Localization Induced by Uniaxial Stress in Pure VO_2, Phys. Rev. Lett. **35**, 873 (1975).

[10] S. A. Corr, D. P. Shoemaker, B. C. Melot, and R. Seshadri, Real-Space Investigation of Structural Changes at the Metal-Insulator Transition in VO_2, Phys. Rev. Lett. **105**, 056404 (2010).

[11] Z. Hiroi, Structural Instability of the Rutile Compounds and its Relevance to the Metal–Insulator Transition of VO_2, Progr. Solid State Chem. **43**, 47 (2015).

[12] K. Jodama, S. Shamoto, H. Harashina, J. Takeda, M. Sato, K. Kakurai, and M. Nishi, Electronic Structure of the Quasi Two-Dimensional Mott System $BaCo_{1-x}Ni_xS_2$, J. Phys. Soc. Jpn. **65**, 1782 (1996).

[13] Z. Guguchia, B. A. Frandsen, D. Santos-Cottin, S. C. Cheung, Z. Gong, Q. Sheng, K. Yamakawa, A. M. Hallas, M. N. Wilson, Y. Cai, J. Beare, R. Khasanov, R. DeRenzi, G. M. Luke, S. Shamoto, A. Gauzzi, Y. Klein, and Y. J. Uemura, Probing the Quantum Phase Transition in Mott Insulator $BaCoS_2$ Tuned by Pressure and Ni Substitution, Phys. Rev. Mater. **3**, 045001 (2019).

[14] T. Sato, H. Kumigashira, D. Ionel, T. Takahashi, I. Hase, H. Ding, J. C. Campuzano, and S. Shamoto, Evolution of Metallic States from the Hubbard Band in the Two-Dimensional Mott System $BaCo_{1-x}Ni_xS_2$, Phys. Rev. B **64**, 075103 (2001).

[15] N. C. Baenziger, L. Grout, L. S. Martinson, and J. W. Schweitzer, $BaCoS_2$, Acta Cryst. C **50**, 1375 (1994).

[16] M. Shatnawi, E. S. Bozin, J. F. Mitchell, and S. J. L. Billinge, Nonpercolative Nature of the Metal-Insulator Transition and Persistence of Local Jahn-Teller Distortions in the Rhombohedral Regime of $La_{1-x}Ca_xMnO_3$, Phys. Rev. B **93**, 165138 (2016).

[17] G. Kresse and J. Furthmuller, Efficient Iterative Schemes for Ab Initio Total-Energy Calculations Using a Plane-Wave Basis Set, Phys. Rev. B **54**, 11169 (1996).

[18] P. E. Blochl, Projector Augmented-Wave Method, Phys. Rev. B **50**, 17953 (1994).

[19] G. Kresse and D. Joubert, From Ultrasoft Pseudopotentials to the Projector Augmented-Wave Method, Phys. Rev. B **59**, 1758 (1999).

[20] J. P. Perdew, K. Burke, and M. Ernzerhof, Generalized Gradient Approximation Made Simple, Phys. Rev. Lett. **77**, 3865 (1996).

[21] J. P. Perdew, A. Ruzsinszky, G. I. Csonka, O. A. Vydrov, G. E. Scuseria, L. A. Constantin, X. Zhou, and K. Burke, Restoring the Density-Gradient Expansion for Exchange in Solids and Surfaces, Phys. Rev. Lett. **100**, 136406 (2008).

[22] See Supplemental Material at [URL will be inserted by

publisher] for the structures used for DFT calculations in this work, as well as calculated band diagrams..

[23] S. L. Dudarev, G. A. Botton, S. Y. Savrasov, C. J. Humphreys, and A. P. Sutton, Electron-Energy-Loss Spectra and the Structural Stability of Nickel Oxide: An LSDA+U Study, Phys. Rev. B **57**, 1505 (1998).

[24] V. M. Zainullina and M. A. Korotin, Ground State of $BaCoS_2$ as a Set of Energy-Degenerate Orbital-Ordered Configurations of Co^{2+} Ions, Phys. Solid State **53**, 978 (2011).

[25] A. Togo and I. Tanaka, First Principles Phonon Calculations in Materials Science, Scr. Mater. **108**, 1 (2015).

[26] S. P. Ong, W. D. Richards, A. Jain, G. Hautier, M. Kocher, S. Cholia, D. Gunter, V. L. Chevrier, K. A. Persson, and G. Ceder, Python Materials Genomics (pymatgen): A Robust, Open-Source Python Library for Materials Analysis, Comput. Mater. Sci. **68**, 314 (2013).

[27] A. A. Coelho, TOPAS and TOPAS-Academic: An Optimization Program Integrating Computer Algebra and Crystallographic Objects Written in C++, J. Appl. Crystallogr. **51**, 210 (2018).

[28] K. Momma and F. Izumi, *VESTA3* for Three-Dimensional Visualization of Crystal, Volumetric and Morphology Data, J. Appl. Crystallogr. **44**, 1272 (2011).

[29] A. P. Hammersley, S. O. Svensson, M. Hanfland, A. N. Fitch, and D. Hausermann, Two-Dimensional Detector Software: From Real Detector to Idealised Image or Two-theta Scan, High Pressure Res. **14**, 235 (1996).

[30] X. Qiu, J. W. Thompson, and S. J. L. Billinge, $PDFgetX2$: a GUI-driven Program to Obtain the Pair Distribution Function from X-ray Powder Diffraction Data, J. Appl. Cryst. **37**, 678 (2004).

[31] C. L. Farrow, P. Juhas, J. W. Liu, D. Bryndin, E. S. B. zin, J. Bloch, T. Proffen, and S. J. L. Billinge, PDFfit2 and PDFgui: Computer Programs for Studying Nanostructure in Crystals, J. Phys.: Condens. Matter **19**, 335219 (2007).

[32] M. G. Tucker, D. A. Keen, M. T. Dove, A. L. Goodwin, and Q. Hui, RMCProfile: Reverse Monte Carlo for Polycrystalline Materials, J. Phys.: Condens. Matter **19**, 335218 (2007).

[33] T. Jurca, A. Farghal, P.-H. Lin, I. Korobkov, M. Murugesu, and D. S. Richeson, Single-Molecule Magnet Behavior with a Single Metal Center Enhanced through Peripheral Ligand Modifications, J. Am. Chem. Soc. **133**, 15814 (2011).

[34] J. Sólyom, Dynamics of crystal lattices, in *Fundamentals of the Physics of Solids: Volume I Structure and Dynamics* (Springer Berlin Heidelberg, Berlin, Heidelberg, 2007) pp. 331–385.

[35] M. T. Dove, Theory of displacive phase transitions in minerals, American Mineralogist **82**, 213 (1997).

[36] M. Born and K. Huang, *Dynamical Theory of Crystal Lattices*, Oxford Classic Texts in the Physical Sciences (Clarendon Press, Oxford, 1954).

[37] L. S. Martinson, J. W. Schweitzer, and N. C. Baenziger, Metal-Insulator Transitions in $BaCo_{1-x}Ni_xS_{2-y}$, Phys. Rev. Lett. **71**, 125 (1993).

SUPPLEMENTARY INFORMATION

Structural Signatures of the Insulator-to-Metal Transition in $BaCo_{1-x}Ni_xS_2$

Emily C. Schueller,[1] Kyle D. Miller,[2] William Zhang,[1] Julia L. Zuo,[1]
James M. Rondinelli,[2] Stephen D. Wilson,[1] and Ram Seshadri[1,3]

[1] *Department of Materials and Materials Research Laboratory, University of California, Santa Barbara, Santa Barbara, CA, 93106*
[2] *Department of Materials Science and Engineering, Northwestern University, Evanston, IL, 60208, USA*
[3] *Department of Chemistry and Biochemistry, University of California, Santa Barbara, Santa Barbara, CA, 93106*

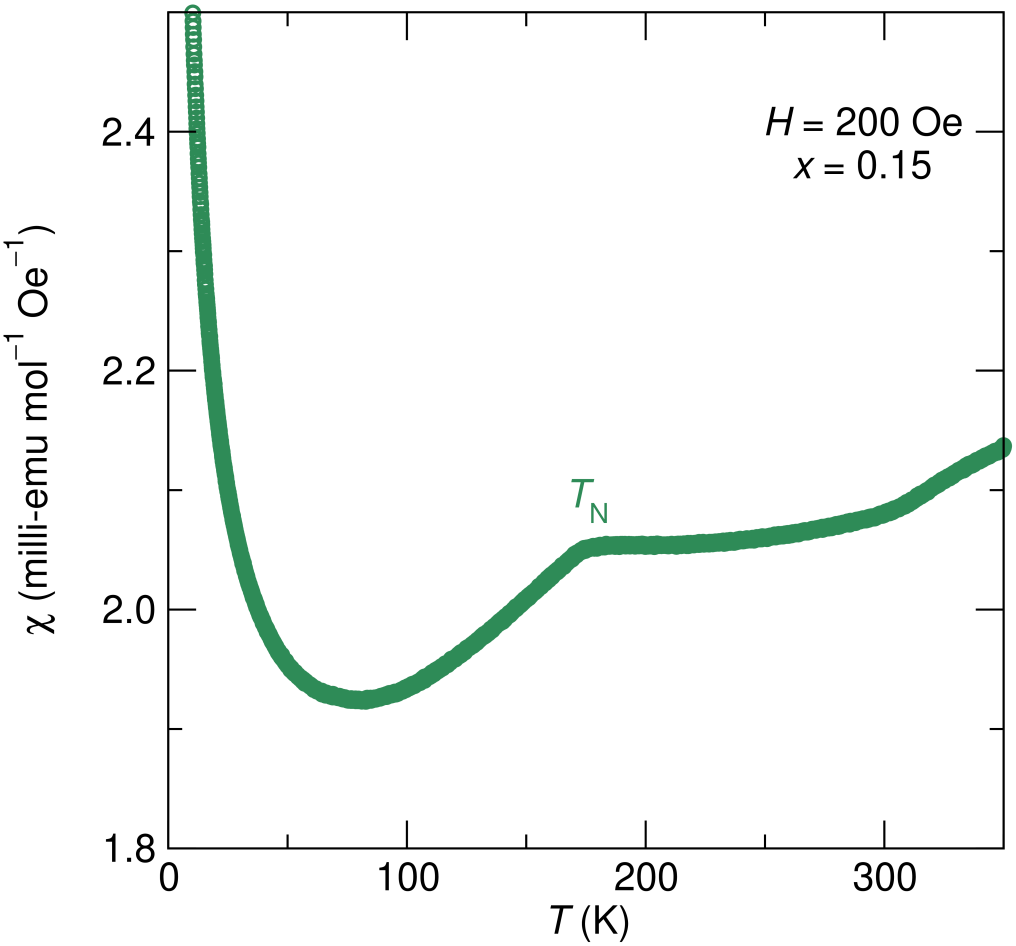

FIG. S1. A magnified plot of temperature–dependent susceptibility for the $x = 0.15$ sample indicates an antiferromagnetic transition around $T = 160$ K.

TABLE S1. XRF results confirm the observed ratio of Co:Ni for the solid solution is close to the nominal composition for all samples, as indicated by the magnetic and electronic properties data. Because XRF was used only as a confirmation, only one data point was taken per sample, and error bars could not be generated.

Nominal Ni (x)	Ni (mol frac)	Co (mol frac)
0.1	0.099	0.901
0.15	0.153	0.847
0.25	0.252	0.748
0.5	0.485	0.515

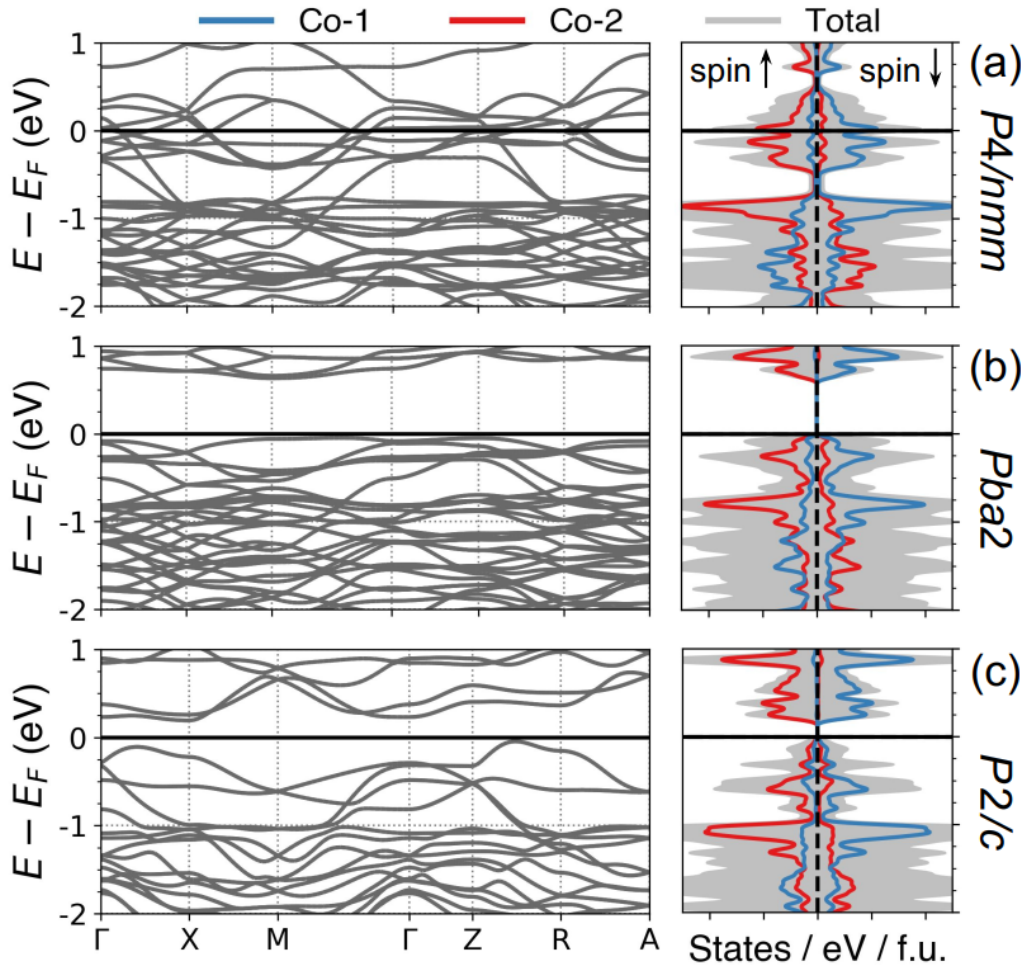

FIG. S2. Electronic band structure (left) and atom-projected density of states (DOS, right) for the (a) $P4/nmm$, (b) $Pba2$, and (c) $P2/c$ structures. Total (gray), spin-up cobalt (blue), and spin-down cobalt (red) are shown. The Fermi level E_F is indicated by a solid horizontal line at 0 eV.

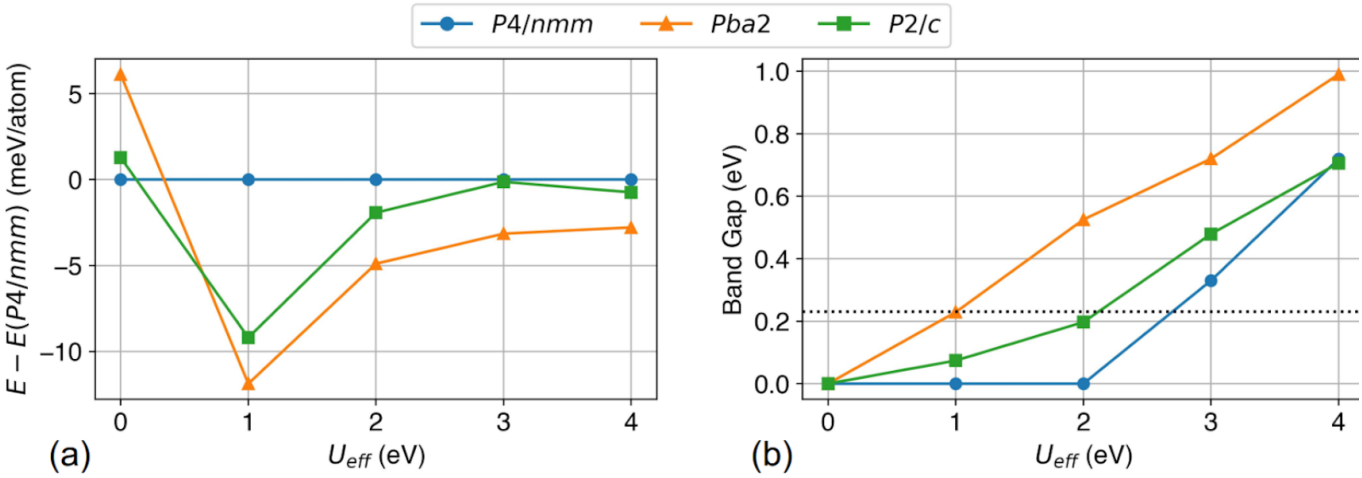

FIG. S3. DFT-PBE+U calculations for different $BaCoS_2$ structures. (a) Relative energy stability with U_{eff} shows that for $U_{\text{eff}} \geq 1$ eV, the $Pba2$ structure is most stable. (b) Band gap dependence on structure symmetry and U_{eff}. $U_{\text{eff}} = 2$ eV gives the best fit between the experimental ground state average structure ($P2/c$) and the band gap approximated from room temperature resistivity measurements [1] (shown as the horizontal dotted line).

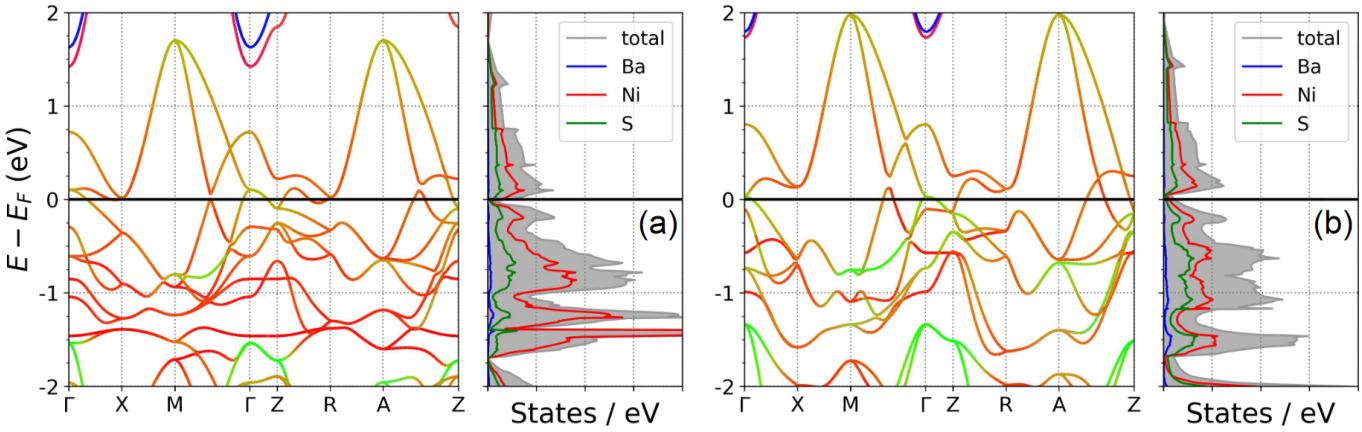

FIG. S4. DFT-PBE electronic band structures and density-of-states for the end member BaNiS2 with (a) $U_{\text{eff}} = 0$ eV and (b) $U_{\text{eff}} = 4$ eV. In both cases, we correctly obtain a metallic state. The projected band character is represented by the color of bands with interpolated coloring indicating mixed character atomic character. These nonmagnetic calculations used structures fully relaxed at the specified U_{eff} value and used a pseudopotential with the following electron configuration for Ni: $3p^6 3d^9 4s^1$. For additional computational details, see the main text.

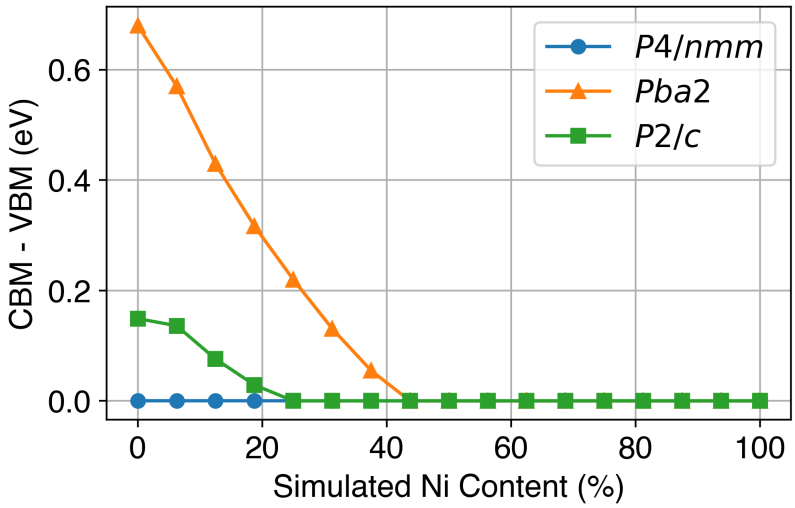

FIG. S5. We disentangle the relative effects of structural and electronic driving forces on the doping-induced IMT by simulating Ni-doping on several structures *via* manipulation of the electron chemical potential. We tracked the energy difference between the bands forming the conduction and valence band edges in the x=0 case for $U_{\text{eff}} = 2$ eV. The doping level at which this energy difference, i.e. CBM-VBM, goes to zero serves as an approximation of the IMT critical point. We find that without any structural distortion ($P4/nmm$ symmetry), $BaCoS_2$ is always metallic due to the existence of the unbroken JT degeneracy. In contrast, the distorted structures, $P2/c$ and $Pba2$, exhibit transitions near $x = 25\%$ and 45% simulated Ni content, respectively. Having established that the $P2/c$ structure features a slight splitting of the JT degeneracy while the $Pba2$ structure features a large splitting of the JT degeneracy, we conclude that the location of the critical point positively correlates with the extent of the splitting. These results indicate that although electron filling induces the IMT, the crystal structure determines the position of the critical point in composition space.

Supplementary Note 1
VASP POSCAR produced by relaxation within the $P4/nmm$ space group. This structure was used in the $U_{\text{eff}} = 2$ eV electronic DOS and band structure calculations. We use a $Z = 8$ structure here for consistency with the $Pba2$ structure size required to accommodate the antiferromagnetic ordering.

```
BaCoS2 - P4/nmm - relaxed
   1.00000000000000
     8.9808179808703148    0.0245970925685161    0.0000000000000000
     0.0245970925685162    8.9808179808703148    0.0000000000000000
     0.0000000000000000    0.0000000000000000    9.0593274061426268
   Ba   Co   S
     8     8    16
Direct
  0.2500000000000000  0.0000000000000000  0.8044065722126641
  0.7500000000000000  0.0000000000000000  0.8044065722126641
  0.2500000000000000  0.5000000000000000  0.8044065722126641
 -0.0000000000000000  0.2500000000000000  0.1955934407873334
  0.5000000000000000  0.2500000000000000  0.1955934407873334
  0.0000000000000000  0.7500000000000000  0.1955934407873334
  0.7500000000000000  0.5000000000000000  0.8044065722126641
  0.5000000000000000  0.7500000000000000  0.1955934407873334
  0.2500000000000000  0.0000000000000000  0.4087978910839780
  0.5000000000000000  0.7500000000000000  0.5912021349160241
 -0.0000000000000000  0.2500000000000000  0.5912021349160241
  0.7500000000000000  0.5000000000000000  0.4087978910839780
  0.5000000000000000  0.2500000000000000  0.5912021349160241
 -0.0000000000000000  0.7500000000000000  0.5912021349160241
  0.7500000000000000 -0.0000000000000000  0.4087978910839780
  0.2500000000000000  0.5000000000000000  0.4087978910839780
  0.2500000000000000 -0.0000000000000000  0.1539865181952868
  0.7500000000000000  0.0000000000000000  0.1539865181952868
  0.2500000000000000  0.5000000000000000  0.1539865181952868
 -0.0000000000000000  0.2500000000000000  0.8460134948047108
  0.5000000000000000  0.2500000000000000  0.8460134948047108
  0.0000000000000000  0.7500000000000000  0.8460134948047108
  0.7500000000000000  0.5000000000000000  0.1539865181952868
  0.5000000000000000  0.7500000000000000  0.8460134948047108
 -0.0000000000000000 -0.0000000000000000  0.5000000000000000
  0.2500000000000000  0.2500000000000000  0.5000000000000000
  0.5000000000000000  0.5000000000000000  0.5000000000000000
  0.7500000000000000  0.7500000000000000  0.5000000000000000
  0.5000000000000000 -0.0000000000000000  0.5000000000000000
  0.2500000000000000  0.7500000000000000  0.5000000000000000
  0.7500000000000000  0.2500000000000000  0.5000000000000000
  0.0000000000000000  0.5000000000000000  0.5000000000000000
```

Supplementary Note 2
VASP POSCAR produced by relaxation within the *Pba*2 space group. This structure was used in the $U_{\text{eff}} = 2$ eV electronic DOS and band structure calculations.

```
BaCoS2 - Pba2 - relaxed
   1.00000000000000
     9.1721952991186733    0.0191229995204385    0.0000000000000000
     0.0980084248266770    9.1716915911111361    0.0000000000000000
     0.0000000000000000    0.0000000000000000    9.0172052128794959
   Ba   Co   S
     8    8   16
Direct
  0.5000000570000012  0.2499999939999995  0.1779467772597982
  0.0000000000000000  0.7499999810000020  0.1779467772597982
  0.0000000000000000  0.2499999939999995  0.1779467772597982
  0.5000000670000020  0.7499999810000020  0.1779467772597982
  0.7500000260000022  0.0000000000000000  0.7816296586861853
  0.7500000360000030  0.4999999870000025  0.7816296586861853
  0.2500000100000008  0.4999999870000025  0.7816296586861853
  0.2500000000000000  0.0000000000000000  0.7816296586861853
  0.2500000000000000  0.0000000000000000  0.3864260687427432
  0.5000000670000020  0.7499999810000020  0.5731355585123694
  0.0000000000000000  0.2499999939999995  0.5731355585123694
  0.7500000360000030  0.4999999870000025  0.3864260687427432
  0.5000000570000012  0.2499999939999995  0.5731355585123694
  0.0000000000000000  0.7499999810000020  0.5731355585123694
  0.7500000260000022  0.0000000000000000  0.3864260687427432
  0.2500000100000008  0.4999999870000025  0.3864260687427432
  0.5000000570000012  0.2499999939999995  0.8270218469486323
  0.0000000000000000  0.7499999810000020  0.8270218469486323
  0.0000000000000000  0.2499999939999995  0.8270218469486323
  0.5000000670000020  0.7499999810000020  0.8270218469486323
  0.7500000260000022  0.0000000000000000  0.1325503963494725
  0.7500000360000030  0.4999999870000025  0.1325503963494725
  0.2500000100000008  0.4999999870000025  0.1325503963494725
  0.2500000000000000  0.0000000000000000  0.1325503963494725
  0.5168349994643364  0.5168012086435567  0.4797948062504105
  0.9831650725356624  0.4831987653564411  0.4797948062504105
  0.2668012146435572  0.2668349424643353  0.4797948062504105
  0.2331987533564401  0.7331649535356632  0.4797948062504105
  0.0168349494643394  0.0168012756435587  0.4797948062504105
  0.4831650305356661  0.9831987003564393  0.4797948062504105
  0.7668012506435602  0.7668349564643364  0.4797948062504105
  0.7331986643564434  0.2331650445356601  0.4797948062504105
```

Supplementary Note 3
VASP POSCAR produced by relaxation within the $P2/c$ space group. This structure was used in the $U_{\text{eff}} = 2$ eV electronic DOS and band structure calculations. We used a $Z = 4$ rather than $Z = 8$ structure here to circumvent symmetry issues encountered in VASP. The relevant physics are unaffected.

```
BaCoS2 - P2/c - relaxed
   1.00000000000000
     6.4448889190635281   -0.3325278857085582    0.0000000000000000
    -0.3441281020049526    6.4670462402178455    0.0000000000000000
     0.0000000000000000    0.0000000000000000    9.0112104666287998
   Ba   Co   S
     4     4     8
Direct
  0.2500000000000000 -0.0000000000000000  0.8036319025971590
  0.7500000000000000  0.0000000000000000  0.1963680974028410
  0.7500000000000000  0.5000000000000000  0.8036319025971590
  0.2500000000000000  0.5000000000000000  0.1963680974028410
  0.2500000000000000 -0.0000000000000000  0.4104180299043749
  0.7500000000000000  0.0000000000000000  0.5895819700956251
  0.7500000000000000  0.5000000000000000  0.4104180299043749
  0.2500000000000000  0.5000000000000000  0.5895819700956251
  0.2500000000000000 -0.0000000000000000  0.1551756212179923
  0.7500000000000000  0.0000000000000000  0.8448243647820065
  0.7500000000000000  0.5000000000000000  0.1551756212179923
  0.2500000000000000  0.5000000000000000  0.8448243647820065
  0.5000000000000000  0.7500000000000000  0.4786188376528286
  0.5000000000000000  0.2500000000000000  0.5213811623471715
 -0.0000000000000000  0.2500000000000000  0.4786188376528286
  0.0000000000000000  0.7500000000000000  0.5213811623471715
```

Supplementary Note 4
VASP POSCAR produced by full atomic relaxation of the primitive cell of the structure in **Supplementary Note 1** using the PBESol functional. This structure was used in the phonon calculations.

```
BaCoS2 relaxed (reference structure) P4/nmm
1.0
      -3.1383970000        -3.1383970000         0.0000000000
      -3.1383970000         3.1383970000         0.0000000000
        0.0000000000         0.0000000000        -8.6776310000
  Ba   Co   S
    2    2   4
Direct
    1.0000000000         0.500000000         0.801165000
    0.5000000000         0.000000000         0.198835000
    1.0000000000         0.500000000         0.410695000
    0.5000000000         0.000000000         0.589305000
    0.0000000000         0.000000000         0.500000000
    0.5000000000         0.500000000         0.500000000
    1.0000000000         0.500000000         0.152575000
    0.5000000000         0.000000000         0.847425000
```

TABLE S2. Crystallographic tables for Rietveld refinements of $BaCo_{1-x}Ni_xS_2$ at $T = 300\,K$.

x	0	0.1	0.15	0.25	0.5	1
Source	11-BM Synchrotron					
Wavelength (Å)	0.45789					
Crystal System	monoclinic	tetragonal				
Space Group (No.)	$P2/c$ (13)	$P4/nmm$ (129)				
a (Å)	4.57605(4)	4.53029(2)	4.51319(4)	4.49098(2)	4.46412(3)	4.43964(3)
b (Å)	8.94234(5)	/				
c (Å)	6.44146(4)	8.93448(6)	8.9328(2)	8.92636(6)	8.9183(2)	8.9122(2)
β (°)	134.7987(5)	/				
Vol (Å^3)	187.039(6)	183.367(3)	181.951(8)	180.035(3)	177.727(6)	175.663(6)
Z	2					
R_{wp} (%)	10.74	14.23	16.38	14.04	12.98	10.68

[1] D. Mandrus, J. L. Sarrao, B. C. Chakoumakos, J. A. Fernandez-Baca, S. E. Nagler, and B. C. Sales, Magnetism in $BaCoS_2$, J. Appl. Phys. **81**, 4620 (1997).